Enhanced efficiency of the Sb$_2$Se$_3$ thin-film solar cell by the anode passivation using an organic small molecular of TCTA

Yujie Hu[1], Zhixiang Chen[1], Yi Xiang[1], Chuanhui Cheng[1, †], Weifeng Liu[2], and Weishen Zhan[1]

[1]School of Physics, Dalian University of Technology, Dalian 116024, China

[2]Mechanical and Electrical Engineering College, Hainan University, Haikou 570228, China

Abstract: Antimony selenide (Sb$_2$Se$_3$) is an emerging solar cell material. Here, we demonstrate that an organic small molecule of 4, 4', 4"-tris(carbazol-9-yl)-triphenylamine (TCTA) can efficiently passivate the anode interface of the Sb$_2$Se$_3$ solar cell. We fabricated the device by the vacuum thermal evaporation, and took ITO/TCTA (3.0 nm)/Sb$_2$Se$_3$ (50 nm)/C$_{60}$ (5.0 nm)/Alq$_3$ (3.0 nm)/Al as the device architecture, where Alq$_3$ is the tris(8-hydroxyquinolinato) aluminum. By introducing a TCTA layer, the open-circuit voltage is raised from 0.36 to 0.42 V, and the power conversion efficiency is significantly improved from 3.2% to 4.3%. The TCTA layer not only inhibits the chemical reaction between the ITO and Sb$_2$Se$_3$ during the annealing process but it also blocks the electron diffusion from Sb$_2$Se$_3$ to ITO anode. The enhanced performance is mainly attributed to the suppression of the charge recombination at the anode interface.

Key words: Sb$_2$Se$_3$; thin-film solar cell; passivation

1. Introduction

Antimony selenide (Sb$_2$Se$_3$) has drawn much attention in the thin-film solar cells community because of its attractive properties such as appropriate band gap, high absorption coefficient, single-phase structure at room temperature, inert grain boundaries, low cost, and low toxicity[1−27]. Moreover, there are only two elements in Sb$_2$Se$_3$, which means that its stoichiometric ratio can be controlled more easily than that of the ternary or quaternary compounds such as CuInGaSe and CuZnSnS(Se). The theoretical power conversion efficiency (PCE) has been predicted to be 26.87% for the Sb$_2$Se$_3$ solar cell[2]. In the past decade the noticeable performance improvements have been achieved. The state-of-the-art Sb$_2$Se$_3$ solar cells have reached efficiencies of ≥10%[3−5]. Various approaches have been developed to fabricate the Sb$_2$Se$_3$ solar cells, such as vacuum thermal evaporation[6, 7], rapid thermal evaporation (RTE)[8, 9], closed-space sublimation (CSS)[10−12], vapor transport deposition (VTD)[13−16], magnetron sputtering (MS)[17−21], pulsed laser deposition[22], hydrothermal deposition (HD)[3, 4, 23], chemical bath deposition (CBD)[5], and spin coating[24, 25]. Among these techniques, vacuum thermal evaporation is one of the techniques that is suitable for large-scale production with a moderate cost. Nevertheless, the PCE of the Sb$_2$Se$_3$ solar cells fabricated by the conventional vacuum evaporation are lower than 5%[6, 7, 28−30], which lags behind that of the device fabricated by the VTD, CSS, RTE, MS, and hydrothermal process.

In solar cell, the extraction and the recombination of the photogenerated charge compete against each other. There-fore, it is of crucial importance to suppress the charge recombination in the cell. In general, it is difficult to avoid the radiative inter-band recombination. What we can do, however, is to inhibit the trap-assisted Shockley–Read–Hall (SRH) recombination that occurrs in the bulk and at the interface. Hence, the interface passivation is one of the important research directions. For example, Al$_2$O$_3$, SiO$_2$, and SiN$_x$ have been used to passivate the electrode interface in the Si solar cells[31, 32]. 4, 4', 4"-tris(carbazol-9-yl)triphenylamine (TCTA) is a small organic molecular, which is often used as the host layer in organic electroluminescence diodes (OLEDs). TCTA has a wide optical bandgap of 3.3 eV. Its lowest unoccupied molecular orbital (LUMO) and highest occupied molecular orbital (HOMO) are located at −2.4 and −5.7 eV, respectively[33]. The TCTA film fabricated by the vacuum thermal evaporation is very smooth and pinhole-free.

In this paper, we fabricated a Sb$_2$Se$_3$ solar cell by the vacuum thermal evaporation, and TCTA was used to passivate the indium tin oxide (ITO)-Sb$_2$Se$_3$ interface. By introducing a 3 nm-thick TCTA layer, the open-circuit voltage (V_{oc}) is improved from 0.36 to 0.42, and the PCE is raised from 3.2% to 4.3%.

2. Results and discussion

Experimental details are given in Supplementary material. Thermogravimetric analysis showed that TCTA experienced a 0.5% weight loss at 440 °C. Under the vacuum condition, the decomposition temperature of TCTA is distinct from that under atmospheric pressure. Therefore, we cannot judge whether or not the TCTA can tolerate the vacuum annealing process at 280 °C. To gauge the impact of the TCTA on the Sb$_2$Se$_3$ film, a series of measurements were performed. Fig. S1 shows the absorption spectra of the Sb$_2$Se$_3$ film deposited on the glass with and without a TCTA layer. As can be

observed, both of the films exhibit a broad absorption from the ultraviolet to the near-infrared region, and there is no discernible difference between the absorption spectra. A Tauc plot is given in the inset of Fig. S1, from which an optical bandgap of 1.1 eV was obtained. This agrees well with the previously reported results[11, 18, 22].

Fig. S2 shows the X-ray diffractions (XRD) patterns of the Sb_2Se_3 films (150 nm) deposited on the ITO substrate with and without a TCTA layer. As can be seen that both of the films show the (020) preferred orientation. The intensity of the (020) diffraction peak is increased from 1636 to 1789 by introducing a TCTA layer, which suggests a very slightly improvement of the crystal quality. Fig. S3 shows the top-view and the cross-sectional scanning electron microscopy (SEM) images of the films. It can be seen that there is no dramatical change after introducing a TCTA layer. Both of the films show a clear grain boundary.

To investigate the impact of the TCTA layer on the ITO-Sb_2Se_3 interface, we performed the X-ray photoelectron spectroscopy (XPS) measurements. The XPS peaks of In $3d_{5/2}$ were given in Supplementary material as Fig. S4. As can be seen, there are two components in the In $3d_{5/2}$ peak for ITO surface. The peaks located at 446.0 and 444.9 eV are assigned to In^{6+} and In^{5+}, respectively. This is consistent with the view that a large amount of oxygen vacancies are presented in ITO, and a portion of indium are incompletely oxidized. However, for the ITO/Sb_2Se_3 (2 nm), the component of In^{6+} disappeared, and a new component appeared at 444.0 eV, which was ascribed to In^{4+}. This result indicates that a portion of indium were reduced to lower valence states after an annealing treatment. In conjunction with the following results of the Sb 3d, it is speculated that a fraction of O were bonded with Sb. Fig. 1 shows the features of Sb $3d_{3/2}$. It can be seen that there is only one component for the 50 nm-thick Sb_2Se_3 film. However, there are two components for the thinner Sb_2Se_3 films. The peak located at around 538.1 eV is originated from the Sb–Se, and the peak located at around 539.6 eV is ascribed to the Sb–O. During the annealing process, the chemical reaction occurred at the ITO–Sb_2Se_3 interface, which give rise to the Sb–O. The ratio of the Sb–O component is decreased from 41% to 17% by introducing a TCTA layer. This result indicates that the TCTA layer can inhibit the chemical reaction occurred at the ITO–Sb_2Se_3 interface, which may reduce the interface defect density. For the case of the thicker Sb_2Se_3 film, the surface is pristine Sb_2Se_3, and there is only one peak of Sb-Se. However, when the Sb_2Se_3 film is very thin, the surface composition is very complicated due to the diffusion and chemical reaction during the annealing treatment. From our previous secondary ion mass spectra measurements, it is known that there are Se, Sb, In, Sn, O, and Na (from glass substrate) elements on the surface[34, 35], and the surroundings of Sb–Se is very different from that for the thicker film. Therefore, the peak location of Sb–Se is different from that of the thicker film.

To access the influence of the TCTA layer on the charge-injection barrier we prepared the device with the architecture of ITO/TCTA (3 nm)/Sb_2Se_3 (50 nm)/NPB (5 nm)/Al, where, NPB is the N, N'-bis(naphthalen-1-yl)-N, N'-bis-(phenyl)benzidine. The device architecture and the molecular structure of NPB are shown in Fig. 2. The control device without a TCTA layer was also fabricated for comparison. The
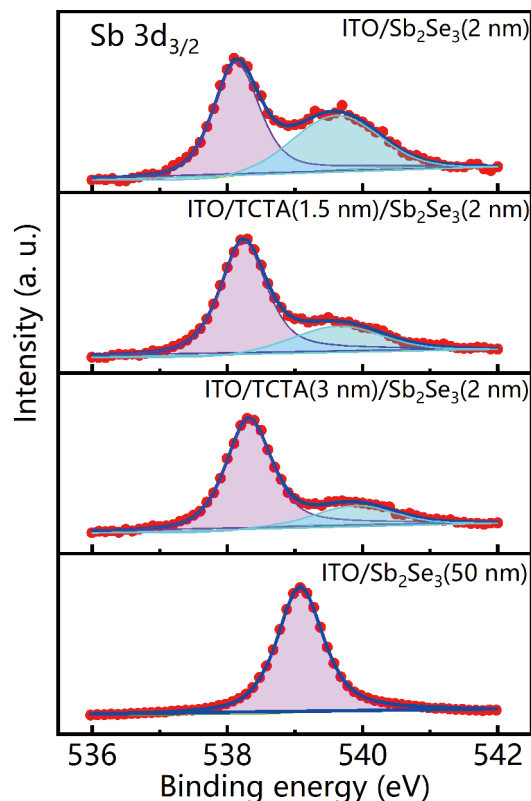

Fig. 1. (Color online) XPS features of the Sb $3d_{3/2}$. The red dots are the experimental data, and the blue lines are the fit results.
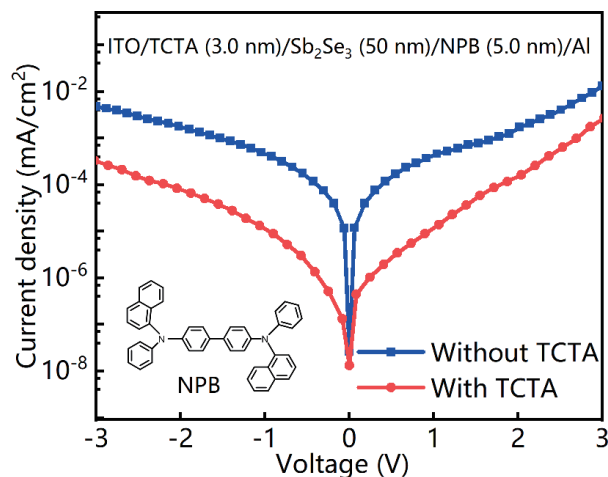

Fig. 2. (Color online) J–V characteristics of the devices with the structure shown in the inset with and without a TCTA layer. The molecular structure of NPB is also given.

LUMO and the HOMO levels of NPB are located at −2.3 and −5.4 eV, respectively, which means that it can block both the electron and the hole injection from the Al electrode. Therefore, the charges in the device are mainly injected from the ITO electrode at lower bias voltage. Fig. 2 shows the current–voltage (J–V) characteristics of the device in the darkness. Here, the positive and negative bias were applied to the ITO electrode. Both the forward and the reverse current densities are decreased by introducing a TCTA layer, which suggests that TCTA can block both the electron and the hole injection from the ITO electrode. This can be ascribed to the higher LUMO level (−2.4 eV) and the lower HOMO level (−5.7 eV) of the TCTA.
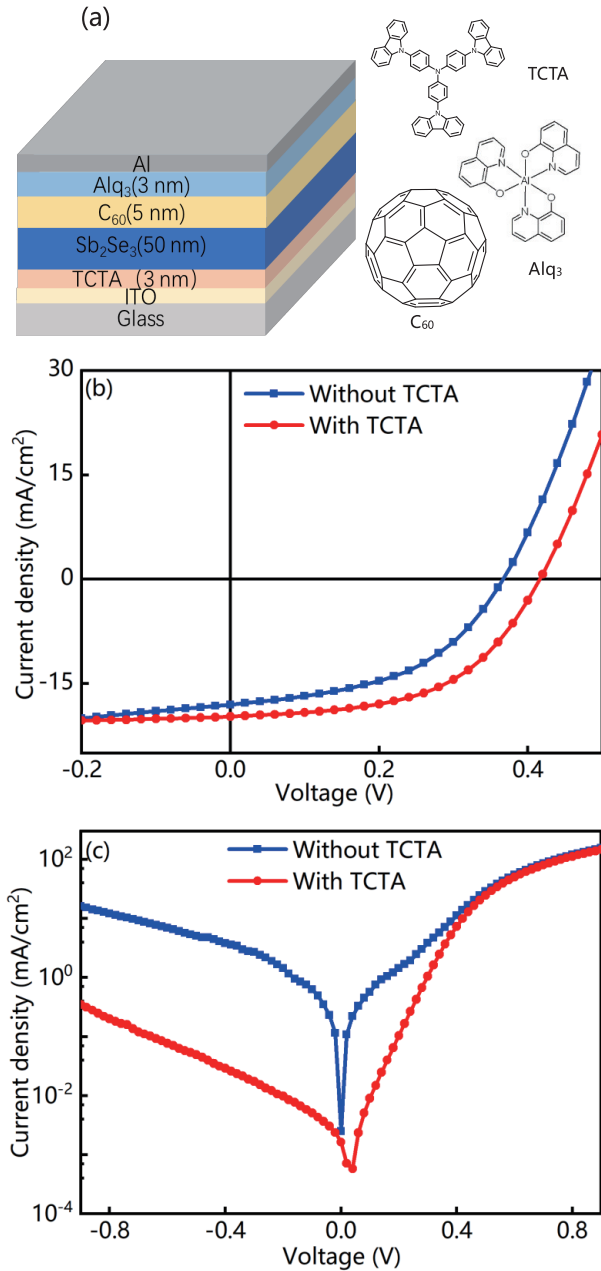
Fig. 3. (Color online) (a) Device architecture and molecular structures. *J–V* characteristics of the devices (b) under one-sun illumination (AM 1.5 100 mW/cm²) and (c) in the darkness.

Next, we prepared the solar cell with an architecture of ITO/TCTA (3.0 nm)/Sb$_2$Se$_3$ (50 nm)/C$_{60}$ (5 nm)/Alq$_3$ (3.0 nm)/Al, where Alq$_3$ is the tris(8-hydroxyquinolinato) aluminum. The device architecture and the molecular structures are shown in Fig. 3(a). The control device without a TCTA layer was also prepared for comparison. Here, C$_{60}$ served as an electron transport layer. An ultra-thin Alq$_3$ layer was used to passivate the cathode interface. The optimal thickness of the TCTA layer was 3.0 nm, and the increase in thickness lead to a deteriorated performance because of its resistance and hole-extraction barrier. Fig. 3(b) shows the *J–V* characteristics of the devices under one-sun illumination (AM 1.5 100 mW/cm²), from which the short-circuit current density (J_{sc}), V_{oc}, fill factor (FF), and PCE were extracted. These parameters are listed in Table 1. By introducing a TCTA layer, the J_{sc} is increased from 18.02 to 19.75 mA/cm², the V_{oc} is raised from 0.36 to 0.42 V, the FF is elevated from 47% to 53%, and the PCE is

enhanced from 3.2% to 4.3%. Fig. 3(c) shows the *J–V* characteristics of the device measured in the darkness. It can be seen that the reverse current is about one order of magnitude smaller than that of the control device, which indicates a reduction in leakage current. The shunt resistance (R_{sh}) and the series resistance (R_s) were obtained from the differential resistance at zero bias and 0.9 V, respectively. The ideality factor (n) and the reverse saturation current density (J_0) can be obtained from the slope and the intercept of the curve of ln($J–V/R_{sh}$) versus $V–JR_s$, respectively. Fig. S5 shows the plots of dV/dJ versus V and ln($J–V/R_{sh}$) versus $V–JR_s$, which are extracted from the *J–V* characteristics measured in the darkness. The fit parameters are summarized in Table 1. As can be seen, the R_{sh} is increased from 0.18 to 23.8 kΩ·cm² by introducing a TCTA layer, which suggests a suppression of the leakage current. The V_{oc} can be described as

$$V_{oc} = \frac{nk_BT}{q} \ln\left(\frac{J_{sc}}{J_0} - 1\right), \quad (1)$$

where k_B is the Bolzmann constant, and T is the absolute temperature[36]. From Eq. (1) it is known that a lower J_0 means a higher V_{oc}. By introducing a TCTA layer, the J_0 is decreased from 1.0×10^{-2} to 8.1×10^{-4} mA/cm², and the ideality factor is reduced from 2.05 to 1.61. The decrease of the J_0 is consistent with the raised V_{oc}, and the reduction in ideality factor suggests a suppression of the trap-assisted SRH recombination.

To reveal the origination of the performance enhancement we investigated the capacitance characteristics of the device. Fig. 4(a) shows the capacitance–frequency (*C–f*) characteristics of the device. It can be seen that both of the devices show a capacitance decrease as the frequency increases. The reason is that less and less charge states can response to the alternating current (AC) voltage as the frequency increases. In addition, the device capacitance is smaller than that of the control device. This result indicates a reduction of the defect state density, which is mainly caused by the anode passivation. According to the abrupt-junction approximation, the device capacitance can be described as

$$\frac{1}{C^2} = \frac{2(V_{bi} - V)}{qA^2\varepsilon_0\varepsilon_rN_a}, \quad (2)$$

where V_{bi} is the built-in potential, A is the device area, ε_0 is the vacuum permittivity, ε_r is the relative dielectric constant, and N_a is the carrier density[37]. We can obtain the built-in potential from the intercept of the Moot-Schottky plot. Fig. 4(b) displays the C^{-2}–V characteristics of the device measured at a frequency of 100 kHz in the darkness. Both of the device exhibit an almost constant capacitance in the bias range −0.8 to 0 V, which indicates a complete depletion of the device. By introducing a TCTA layer, the V_{bi} is increased from 0.46 to 0.52 V, which is consistent with the raised V_{oc}.

To further elucidate the mechanism behind the device performance improvement, we measured the impedance spectroscopy of the device at a bias of 0.2 V in darkness. Fig. 5(a) shows the Nyquist plots, where Z' and Z'' are the real and imaginary components of the impedance, respectively. The impedance data are fitted by Zview using an equivalent circuit model shown in Fig. 5(a), and the fit parameters are sum-

Table 1.   Performance parameters of the devices.

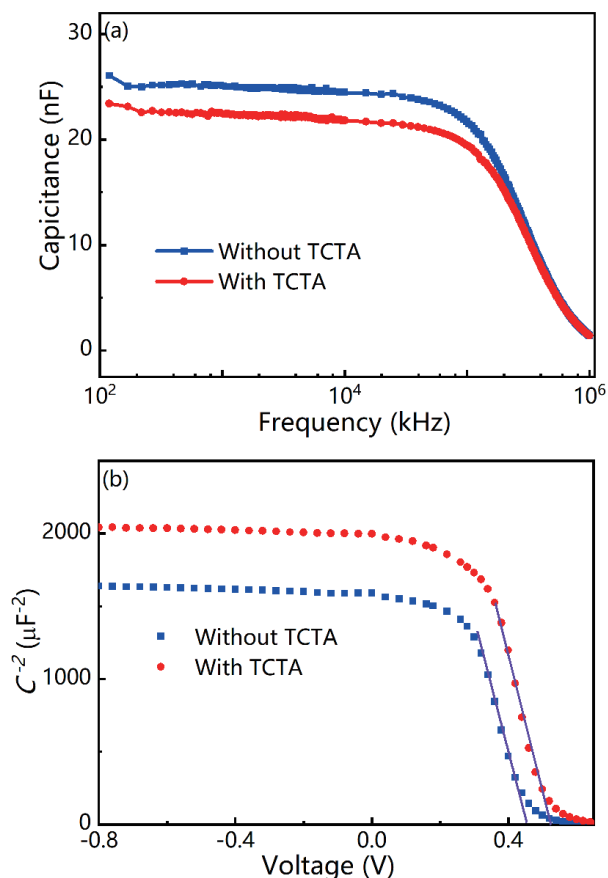| Cell structure	V_{oc} (V)	J_{sc} (mA/cm²)	FF	R_s (Ω·cm²)	R_{sh} (kΩ·cm²)	J_0 (mA/cm²)	n	PCE (%)
With TCTA	0.42	19.75	0.53	2.9	23.8	8.1×10^{-4}	1.61	4.3
Without TCTA	0.36	18.02	0.48	2.8	0.18	1.0×10^{-2}	2.05	3.2

Fig. 4. (Color online) (a) C–f characteristics of the devices at 0 V bias in the darkness. (b) C^{-2}–V characteristics of the device at 100 kHz in the darkness.
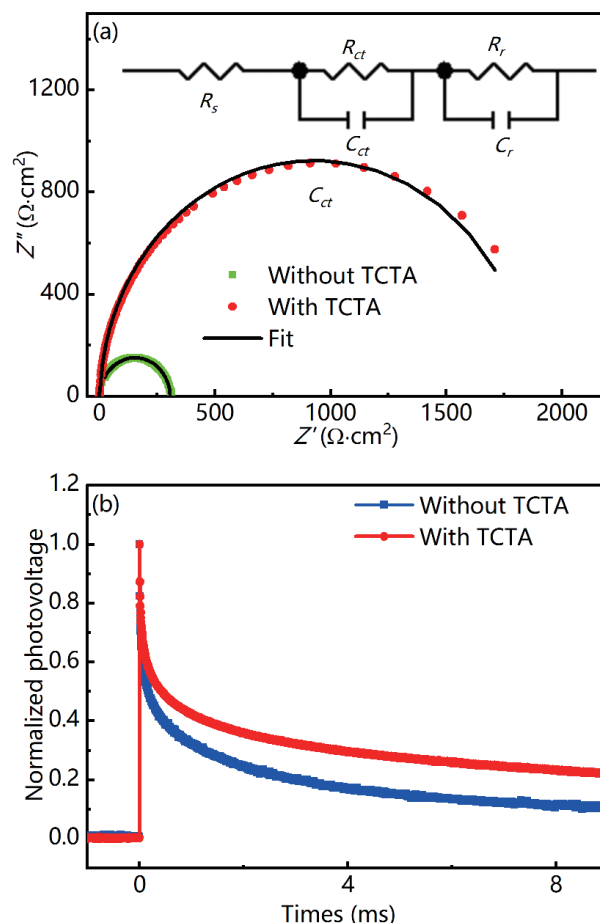

Fig. 5. (Color online) (a) Nyquist plots of the impedance spectra measured at a bias of 0.2 V in the darkness. The equivalent circuit model is also given. (b) Normalized transient photovoltage of the device with and without a TCTA layer.

marized in Table 2. There are three components in this model. R_s is used to describe the series resistance. R_{ct} and C_{ct} are connected in parallel to characterize the device at high frequency, which reflects the charge transport in the device. And R_r and C_r are connected in parallel to characterize the device at low frequency, which represents the charge recombination in the device. It can be seen that R_{ct} is increased from 3.0 to 5.6 Ω·cm² by introducing a TCTA layer, which is caused by the resistance and the hole-injection barrier introduced by the TCTA layer. However, R_r is significantly increased from 301 to 1846 Ω·cm², which suggests that charge recombination in the device is significantly suppressed. We also measured the transient photovoltage (TPV), and the results are shown in Fig. 5(b). By introducing a TCTA layer, the half-life is increased from 1.65×10^{-4} to 4.25×10^{-4} s, which suggests an inhibition of the charge recombination. This result is consistent with the above impedance analysis.

Let us now turn to the external quantum efficiency (EQE) spectra of the device. Fig. 6 shows the EQE spectra of the devices. Both of the devices demonstrate a wide spectral response up to 1000 nm. Both of the spectra display a valley at around 500 nm, which results from the weak light absorption in this region caused by the thin-film interference effect.

The device with a TCTA layer has a higher EQE in 400–1000 nm compared to that of the control device. The recombination at ITO-Sb₂Se₃ interface was suppressed by introducing a TCTA layer. Consequently, the charge extraction efficiency and the J_{sc} were improved, which gave rise to the increase in EQE. An EQE maximum of 74% was obtained at 435 nm on the device with a TCTA layer. And an EQE maximum of 72% was obtained at 400 nm on the control device. By integrating the EQE with the standard AM 1.5 solar spectrum, J_{sc} of 19.64 and 18.05 mA/cm² were achieved for the devices with and without a TCTA layer, respectively. These are very close to the values extracted from the J–V measurements under illumination.

The repeatability and the stability of the device were investigated. We fabricated 69 solar cells. Fig. S6 displays the distribution of the PCEs, which shows a normal distribution with an average of 3.6 % and a variance of 0.47%. The device stability was tested without encapsulation. The PCE had a ~30% loss after a storage in air at 25 °C and 30% relative humidity for 24 h. This problem is primarily caused by the organic materials, and can be partially overcome by encapsulation.

Y J Hu et al.: Enhanced efficiency of the Sb₂Se₃ thin-film solar cell by the anode passivation ......

Table 2. Fit parameters of the impedance spectra.

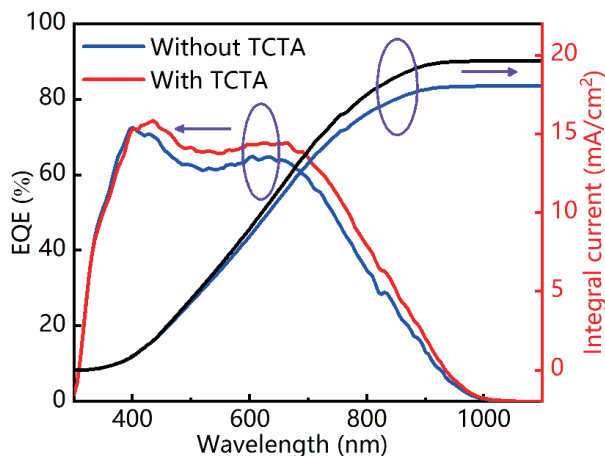| Cell structure	R_s ($\Omega \cdot cm^2$)	R_{ct} ($\Omega \cdot cm^2$)	R_r ($\Omega \cdot cm^2$)	C_{ct} (10^{-6} F/cm^2)	C_r (10^{-7} F/cm^2)
With TCTA	2.2	3.0	301	4.1	2.9
Without TCTA	2.4	5.6	1846	2.8	2.8

Fig. 6. (Color online) EQE spectra and the integral current of the devices.

To clarify the role of the oxygen in Sb$_2$Se$_3$ film, we performed the following experiments. The ITO substrate was treated by oxygen plasma before device fabrication, which can increase the oxygen level on the ITO surface, and consequently increase the work function of the ITO anode. The increase in anode work function would enhance the hole collection and the device PCE. However, the device efficiency was decreased from 4.3% to 3.9% and from 3.2% to 2.8% for the devices with and without a TCTA layer, respectively, after the oxygen plasma treatment. The result is shown in Fig. S7 in Supplementary Material. This result is similar to that reported by Liu *et al.*[38], who found that the device performance is deteriorated by adding oxygen in Sb$_2$Se$_3$ film near the anode. However, the PCE is increased by adding oxygen in Sb$_2$Se$_3$ film near the n-type layer.

The lower PCE of the Sb$_2$Se$_3$ solar cells fabricated by the conventional vacuum evaporation is mainly caused by two reasons: the first is the relatively higher defect density, which may lead to the trap-assisted recombination; and the second is the (020) oriented film, which is not favored for the carrier transport. To improve the device performance the innovations are required in the following directions. It is fundamental to regulate the film deposition kinetics to suppress the defect formation and realize the (001) oriented film. It is also important to select better electron and hole transport layers. In addition, increase of the carrier density by doping may further improve the efficiency of device.

3. Conclusions

We have demonstrated that a small organic molecule of TCTA can efficiently passivate the ITO–Sb$_2$Se$_3$ interface in the Sb$_2$Se$_3$ solar cell fabricated by the vacuum thermal evaporation. By adding a TCTA layer, the V_{oc} is raised from 0.36 to 0.42 V, and the PCE is significantly increased from 3.2% to 4.3%. The introduction of a TCTA layer does not significantly alter the properties of the Sb$_2$Se$_3$, and there are two major reasons for the enhancement of the device performance. First,

the TCTA layer can block the electron diffusion from Sb$_2$Se$_3$ to ITO anode, and the interface recombination is therefore inhibited. Second, the chemical reaction between the ITO and Sb$_2$Se$_3$ is inhibited by introducing a TCTA layer, which may reduce the interface state density. The drawback is that the hole-extraction barrier is slightly raised by introducing a TCTA layer. This work provides a method to improve the performance of the Sb$_2$Se$_3$ solar cell.

Acknowledgements

Appendix A. Supplementary materials

Supplementary materials to this article can be found online at https://doi.org/10.1088/1674-4926/44/8/082701.

References

[1] Li Z Q, Liang X Y, Li G, et al. 9.2%-efficient core-shell structured antimony selenide nanorod array solar cells. Nat Commun, 2019, 10, 125

[2] Jiménez T, Seuret-Jiménez D, Vigil-Galán O, et al. Sb$_2$(S$_{1-x}$e$_x$)$_3$ solar cells: The impact of radiative and non-radiative loss mechanisms. J Phys D, 2018, 51, 435501

[3] Tang R F, Wang X M, Lian W T, et al. Hydrothermal deposition of antimony selenosulfide thin films enables solar cells with 10% efficiency. Nat Energy, 2020, 5, 587

[4] Zhao Y Q, Wang S Y, Jiang C H, et al. Regulating energy band alignment via alkaline metal fluoride assisted solution post-treatment enabling Sb$_2$(S, Se)$_3$ solar cells with 10.7% efficiency. Adv Energy Mater, 2022, 12, 2103015

[5] Zhao Y Q, Wang S Y, Li C, et al. Regulating deposition kinetics *via* a novel additive-assisted chemical bath deposition technology enables fabrication of 10.57%-efficiency Sb$_2$Se$_3$ solar cells. Energy Environ Sci, 2022, 15, 5118

[6] Luo M, Leng M Y, Liu X S, et al. Thermal evaporation and characterization of superstrate CdS/Sb$_2$Se$_3$ solar cells. Appl Phys Lett, 2014, 104, 173904

[7] Kumar V, Artegiani E, Punathil P, et al. Analysis of Se Co-evaporation and post-selenization for Sb$_2$Se$_3$-based solar cells. ACS Appl Energy Mater, 2021, 4, 12479

[8] Zhou Y, Wang L, Chen S Y, et al. Thin-film Sb$_2$Se$_3$ photovoltaics with oriented one-dimensional ribbons and benign grain boundaries. Nat Photonics, 2015, 9, 409

[9] Ishaq M, Deng H, Yuan S J, et al. Efficient double buffer layer Sb$_2$(Se$_x$S$_{1-x}$)$_3$ thin film solar cell via single source evaporation. Sol RRL, 2018, 2, 1800144

[10] Li D B, Yin X X, Grice C R, et al. Stable and efficient CdS/Sb$_2$Se$_3$ solar cells prepared by scalable close space sublimation. Nano Energy, 2018, 49, 346

[11] Hutter O S, Phillips L J, Durose K, et al. 6.6% efficient antimony selenide solar cells using grain structure control and an organic contact layer. Sol Energy Mater Sol Cells, 2018, 188, 177

[12] Li G, Li Z Q, Liang X Y, et al. Improvement in Sb$_2$Se$_3$ solar cell efficiency through band alignment engineering at the buffer/absorber interface. ACS Appl Mater Interfaces, 2019, 11, 828

[13] Tao J H, Hu X B, Guo Y X, et al. Solution-processed SnO_2 interfacial layer for highly efficient Sb_2Se_3 thin film solar cells. Nano Energy, 2019, 60, 802

[14] Kondrotas R, Zhang J, Wang C, et al. Growth mechanism of Sb_2Se_3 thin films for photovoltaic application by vapor transport deposition. Sol Energy Mater Sol Cells, 2019, 199, 16

[15] Wen X X, Chen C, Lu S C, et al. Vapor transport deposition of antimony selenide thin film solar cells with 7.6% efficiency. Nat Commun, 2018, 9, 2179

[16] Liang G X, Chen M D, Ishaq M, et al. Crystal growth promotion and defects healing enable minimum open-circuit voltage deficit in antimony selenide solar cells. Adv Sci, 2022, 9, e2105142

[17] Liang G X, Zhang X H, Ma H L, et al. Facile preparation and enhanced photoelectrical performance of Sb_2Se_3 nano-rods by magnetron sputtering deposition. Sol Energy Mater Sol Cells, 2017, 160, 257

[18] Liang G X, Zheng Z H, Fan P, et al. Thermally induced structural evolution and performance of Sb_2Se_3 films and nanorods prepared by an easy sputtering method. Sol Energy Mater Sol Cells, 2018, 174, 263

[19] Tang R, Chen S, Zheng Z, et al. Heterojunction annealing enabling record open-circuit voltage in antimony triselenide solar cells. Adv Mater, 2022, 34, 2109078

[20] Lin J H, Mahmood A, Chen G J, et al. Crystallographic orientation control and defect passivation for high-efficient antimony selenide thin-film solar cells. Mater Today Phys, 2022, 27, 100772

[21] Chen S, Liu T X, Chen M D, et al. Crystal growth promotion and interface optimization enable highly efficient Sb_2Se_3 photocathodes for solar hydrogen evolution. Nano Energy, 2022, 99, 107417

[22] Mavlonov A, Shukurov A, Raziq F, et al. Structural and morphological properties of PLD Sb_2Se_3 thin films for use in solar cells. Sol Energy, 2020, 208, 451

[23] Wang W H, Wang X M, Chen G L, et al. Promising $Sb_2(S,Se)_3$ solar cells with high open voltage by application of a TiO_2/CdS double buffer layer. Sol RRL, 2018, 2, 1800208

[24] Choi Y C, Lee Y H, Im S H, et al. Efficient inorganic-organic heterojunction solar cells employing $Sb_2(S_x/Se_{1-x})$ graded-composition sensitizers. Adv Energy Mater, 2014, 4, 1301680

[25] Zhou Y, Leng M Y, Xia Z, et al. Solution-processed antimony selenide heterojunction solar cells. Adv Energy Mater, 2014, 4, 1301846

[26] Wang L, Li D B, Li K H, et al. Stable 6%-efficient Sb_2Se_3 solar cells with a ZnO buffer layer. Nat Energy, 2017, 2, 1

[27] Chen S, Liu T X, Zheng Z H, et al. Recent progress and perspectives on Sb_2Se_3-based photocathodes for solar hydrogen production via photoelectrochemical water splitting. J Energy Chem, 2022, 67, 508

[28] Park S N, Kim S Y, Lee S J, et al. Controlled synthesis of (hk1) preferentially oriented Sb_2Se_3 rod arrays by co-evaporation for photovoltaic applications. J Mater Chem A, 2019, 7, 25900

[29] El Radaf I M. Structural, optical, optoelectrical and photovoltaic properties of the thermally evaporated Sb_2Se_3 thin films. Appl Phys A, 2019, 125, 1

[30] Kumar V, Artegiani E, Kumar A, et al. Effects of post-deposition annealing and copper inclusion in superstrate Sb_2Se_3 based solar cells by thermal evaporation. Sol Energy, 2019, 193, 452

[31] Black L E, van de Loo B W H, Macco B, et al. Explorative studies of novel silicon surface passivation materials: Considerations and lessons learned. Sol Energy Mater Sol Cells, 2018, 188, 182

[32] Bonilla R S, Hoex B, Hamer P, et al. Dielectric surface passivation for silicon solar cells: A review. Phys Status Solidi A, 2017, 214, 1700293

[33] Wu R X, Liu W Q, Wang Z, et al. Highly efficient solution-processed white organic light-emitting diodes based on a co-host system by controlling energy transfer among different emitters. J Mater Chem C, 2022, 10, 5648

[34] Cheng C H, Li M, Song H Q, et al. Enhanced performance of the Sb_2Se_3 thin-film solar cell by organic molecule-induced crystallization and suppression of the interface recombination. ACS Appl Energy Mater, 2021, 4, 5079

[35] Li W H, Li M, Hu Y J, et al. Enhanced performance of antimony selenide thin film solar cell using PbI_2 as a dopant. Appl Phys Lett, 2021, 118, 093903

[36] Nelson J. The physics of solar cells. London: Imperial College Press, 2003

[37] Neamen D. Semiconductor physics and devices: basic principles. 4th ed. New York: McGraw Hill, 2011

[38] Liu X S, Chen C, Wang L, et al. Improving the performance of Sb_2Se_3 thin film solar cells over 4% by controlled addition of oxygen during film deposition. Prog Photovolt: Res Appl, 2015, 23, 1828

Yujie Hu is a master student at School of Physics, Dalian University of Technology. She received her BS from Jining University in 2019. Her research focuses on solar cells.

Chuanhui Cheng is an associate professor at School of Physics, Dalian University of Technology. He received his PhD from National Integrated Optoelectronics laboratory, College of Electronic Science and Engineering, Jilin University, in 2007. His research focuses on solar cells.